Polymer Testing 156 (2026) 109107

Contents lists available at ScienceDirect

Polymer Testing

journal homepage: www.elsevier.com/locate/polytest

Investigating the uniaxial compressive mechanics of graded polymer foams via *in-situ* synchrotron X-ray microtomography

Paolo Iaccarino [a,b,c,*], Clément Rey [d], Lorenzo Miele [b,c], Victor Okumko [e,f], Mario Scheel [e], Timm Weitkamp [e], Henry Proudhon [f], Ferdinando Auricchio [g], Ernesto Di Maio [b,c], Andrei Constantinescu [d,*]

[a] Scuola Superiore Meridionale, Largo San Marcellino 10, Naples, 80138, Italy
[b] Dipartimento di Ingegneria Chimica, dei Materiali e della Produzione Industriale, University of Naples Federico II, P.le Tecchio 80, Naples, 80125, Italy
[c] foamlab, University of Naples Federico II, P.le Tecchio 80, Naples, 80125, Italy
[d] Laboratoire de Mécanique des Solides, CNRS, École Polytechnique, Institut Polytechnique de Paris, Palaiseau, 91128, France
[e] Synchrotron SOLEIL, L'Orme des Merisiers, Départementale 128, 91190, Saint-Aubin, France
[f] MINES ParisTech, PSL University, MAT - Centre des Matériaux, CNRS UMR 7633, BP 87, Evry, 91003, France
[g] Dipartimento di Ingegneria Civile e Architettura, University of Pavia, Via Ferrata 3, Pavia, 27100, Italy

ARTICLE INFO

Keywords:
Batch foaming
Polypropylene
Functionally graded
Micromechanics
Uniaxial compression

ABSTRACT

Graded polymer foams are emerging as transformative materials for structural applications, outperforming uniform foams due to their spatially tailored density and microstructural features. However, harnessing their full potential requires a deep understanding of how their macroscopic mechanical behavior relates to their complex microstructure evolution. In this study, we elucidate the uniaxial compressive response of graded foams using *in-situ* synchrotron X-ray microtomography, complemented by comparative experiments on uniform foams of varying densities. Our findings reveal that graded foams exhibit both qualitatively and quantitatively distinct mechanical behavior, driven by unique microscale deformation mechanisms. We evaluate and discuss their superior energy absorption performance and demonstrate how the density, cell size and circularity profile evolves under increasing macroscopic strain. Notably, the graded architecture enables precise control over the localization and progression of densification bands, offering unprecedented design flexibility for advanced structural applications.

1. Introduction

Graded polymer foams—hereafter referred to as graded foams—are rapidly emerging as high-performance alternatives to spatially uniform foams [1]. Unlike their uniform counterparts, graded foams exhibit continuous spatial variations in density and/or microstructural features, such as cell size or wall/strut thickness distributions. It is important to distinguish graded foams from layered foams, which exhibit discrete, step-wise changes in density and microstructure—often in a single direction—and are typically fabricated by gluing or soldering layers of uniform foams [2,3].

Graded polymer foams exhibit significant potential in energy absorption applications, as they enable the customization of their constitutive behavior, for example, through the design of the density map [4]. In fact, density is the primary factor influencing the mechanical properties of polymer foams [5]. However, the challenges associated with the production of graded foams have limited research primarily to theoretical and/or numerical investigations [6–10], with only a few recent experimental studies successfully producing graded foams using additive manufacturing [11–13].

Nevertheless, producing a graded foam using additive manufacturing is not always the optimal choice, as it is challenging to reproduce the statistical features (e.g., cell size, cell orientation distributions) of polymer foams. Furthermore, additive manufacturing processes are typically significantly slower than the conventional gas foaming methods employed in industrial applications. Finally, during additive manufacturing, the strain histories are typically bland. In contrast, in gas foaming methods, the extreme strains and strain rates to which the material is subjected serve as fundamental processing tools for enhancing the performance of the base polymer within the cell walls and struts of the resulting foam.

A technology that overcomes these limitations has been introduced by Trofa et al. [14] to produce graded polymeric foams based on time-varying boundary conditions in gas foaming [14]. This technology can

* Corresponding authors.
E-mail addresses: paolo.iaccarino@unina.it (P. Iaccarino), andrei.constantinescu@polytechnique.edu (A. Constantinescu).

https://doi.org/10.1016/j.polymertesting.2026.109107
Received 23 October 2025; Received in revised form 8 January 2026; Accepted 3 February 2026
Available online 11 February 2026

be coupled with mechanical constraints and complex preform geometries and has been demonstrated to efficiently produce graded foams with topologically optimized density maps to fulfill targeted structural requirements [1].

To effectively design the density map, a thorough understanding of the micromechanical phenomena underlying macroscopic mechanical behavior is essential. To the best of our knowledge, both the micromechanics and macromechanics of graded foams remain largely unexplored.

Microtomography (μCT) has been widely utilized as a tool to characterize the microstructure of uniform polymer foams *per se* [15,16], but only a limited number of studies have employed this technique *in-situ* to investigate the relationship between mechanical behavior and micromechanical phenomena [17–19]. In fact, it is well established that the macroscopic mechanical behavior of foams arises from complex symmetric and asymmetric deformation micromechanisms, including the bending and elastic or plastic buckling of cell walls and struts [5]. Observing these micromechanisms is, therefore, essential for developing a deeper understanding and for proposing more accurate, physics-based multiscale models to predict their mechanical properties.

Besides laboratory X-ray sources, synchrotron radiation (SR) has proved particularly useful for μCT studies on polymer foams, owing not only to the high intensity of SR X-rays, which enables *in-situ* measurements at high resolution in reasonable time, but also because the degree of spatial coherence of SR gives access to inline phase contrast and thus to drastically increased signal for light elements such as those constituting most polymers [20].

The first uniaxial compression studies via *in-situ* synchrotron microtomography on polymer foams were conducted around the turn of the millennium, just after SR-based μCT (SRμCT) had become available, when Elliott et al. [21] characterized open-cell polyurethane foams by *in-situ* compression SRμCT up to 80% compressive strain. The deformation process was shown to occur homogeneously throughout the foam up to a compressive strain of approximately 6%, where collapsed bands of denser material began to form in correspondence with a dramatic loss of tangent stiffness in the stress–strain curve. Importantly, the authors also observed the formation of a collapse band around a particular foam cell that was significantly larger than its immediate neighbors; however, this was not an isolated buckling transition but rather a cooperative collapse involving an entire layer of connected cells of considerable extent [21]. Youssef et al. [22] conducted *in-situ* uniaxial compression SRμCT measurements up to 20% to analyze the deformation mechanisms in a closed-cell polyurethane (PU) foam and to validate a finite element analysis (FEA) modeling procedure [22]. Their FEA reveals that plastic yielding mechanisms take place at a very early stage of macroscopic deformation: in fact, the first yielding point appears at 0.1% of (macroscopic) strain, which is still in the apparently linear domain of the macroscopic behavior; moreover, the authors numerically observed that at large strain an important part of the foam still behaves elastically [22]. Adrien et al. [23] studied the damage evolution of syntactic foams with different matrices (epoxy, polypropylene (PP), and PU) in confined compression via *in-situ* SRμCT measurements, finding that when the matrix is softer (PP and PU) the damage is homogeneously distributed, while for a stiffer matrix (epoxy) the damage is localized in bands [23]. Roux et al. [24] conducted *in-situ* compression SRμCT measurements on PP bead foams up to 30% strain combined with digital image correlation to reveal the heterogeneity of the strain field at both the cell (microscopic, μm) and bead (mesoscopic, mm) scales [24]. Chai et al. [25] investigated the micromechanics of the struts and walls of a closed-cell polymethacrylimide (PMI) foam under uniaxial compression with *in-situ* SRμCT and digital volume correlation, highlighting the correlation between cell wall buckling and deformation bending for closed-cell foams [25]. In a later work, Chai et al. [26] revealed different types (discrete or spreading) of deformation banding for PMI foams with different densities and concluded that elastic buckling of cell walls dominates cell collapse, and the buckling strength of walls highly depends on their thickness and inclination angles with respect to the loading direction [26].

In conclusion, the integration of uniaxial compression tests and *in-situ* SRμCT has significantly enhanced our understanding of the relationship between microstructure and macroscopic mechanical properties in uniform polymer foams.

Within this framework, the aim of the present work is to unveil the mechanics of graded foams simultaneously at both the microscale and macroscale, thereby enhancing the understanding of the *microstructure–property* relationship in these novel polymer foams. To achieve this goal, we first design and produce a graded foam with a density gradient via batch foaming through the recent technology introduced by Trofa et al. [14] coupled with mechanical constraints. Subsequently, we produce two uniform foams: one with a density comparable to the average density of the graded foam and the other with a lower density — the latter to provide a comparison for the lower density regions of the graded foam. We then investigate the mechanics of these three foams at both the microscale and macroscale simultaneously during uniaxial compression experiments using *in-situ* SRμCT. We study the energy absorption performance of the foams, and we compute their density and cell size profiles at different levels of (macroscopic) strain.

The present work is organized as follows: Section 2 reports the materials utilized and the procedures employed to produce the graded and uniform foams; Section 3 provides information on the experimental setup and the protocol used for the uniaxial compression measurement with *in situ* SRμCT; Section 4 presents the analysis of (i) the energy absorption performance, (ii) the density profiles at different levels of strain, (iii) microstructural details and (iv) the diameter and circularity profiles at different levels of strain of the foams, along with a discussion of these points; Section 5 summarizes the findings of the present work and suggests possible directions for future research.

2. Materials and foamed samples production

Polypropylene (PP, code E02ES) with a density of $\rho^{PP} = 905$ kg/m^3 is provided by Sinopec Zhenhai Refining & Chemical Company (Zhejiang Province, China) in the form of a slab 16 mm thick. The slab is machined into cylindrical preforms of bulk PP using a numerically controlled milling machine (MDX-40, Roland DG Corporation, Hamamatsu-shi, Shizuoka-ken, Japan). Three types of cylindrical preforms are produced, with diameter d and height h: type p-U, with $d = 6.7$ mm and $h = 6.7$ mm, which will be used to produce the uniform (U) foams; type p-ULD, with $d = 5.7$ mm and $h = 5.0$ mm, which will be used to produce the uniform low density (ULD) foams; type p-G, with $d = 10$ mm and $h = 3$ mm, which will be used to produce the graded (G) foams. To produce foams, we used CO_2 (purity 99.99%) as a blowing agent, supplied by SOL S.p.A. (Monza, Italy).

The foaming apparatus is a 0.3 L thermoregulated pressure vessel (model BC-1, High Pressure Equipment Co., Erie, PA, USA). The electrical heater is controlled by a PID thermoregulator (mod. 1850, Gefran S.p.A., Provaglio d'Iseo, Brescia, Italy), which takes as input the temperature of the heating jacket using a type J thermocouple. The temperature of the sample inside the vessel is measured using a Pt100 temperature sensor (Gefran S.p.A., Provaglio d'Iseo, Brescia, Italy). A pressure transducer (model TK, Gefran S.p.A., Provaglio d'Iseo, Brescia, Italy) is used to measure pressure during the saturation step. The pressure discharge system consists of a discharge ball valve (model 15-71 NFB, High Pressure Equipment Co., Erie, PA, USA) and an electromechanical actuator (model 15-72 NFB TSR 8, High Pressure Equipment Co., Erie, PA, USA). The pressure drop rate (PDR) is measured by a programmable logic controller (SIMATIC S7-1200 CPU, Siemens, Munich, Germany) with a sampling rate $\tau_m = 1$ ms, following the procedure proposed by Miele et al. [27]. A more detailed description of the experimental setup and of the described configuration can be found in Iaccarino et al. [28].

The foams are produced as illustrated in Fig. 1 and described below.

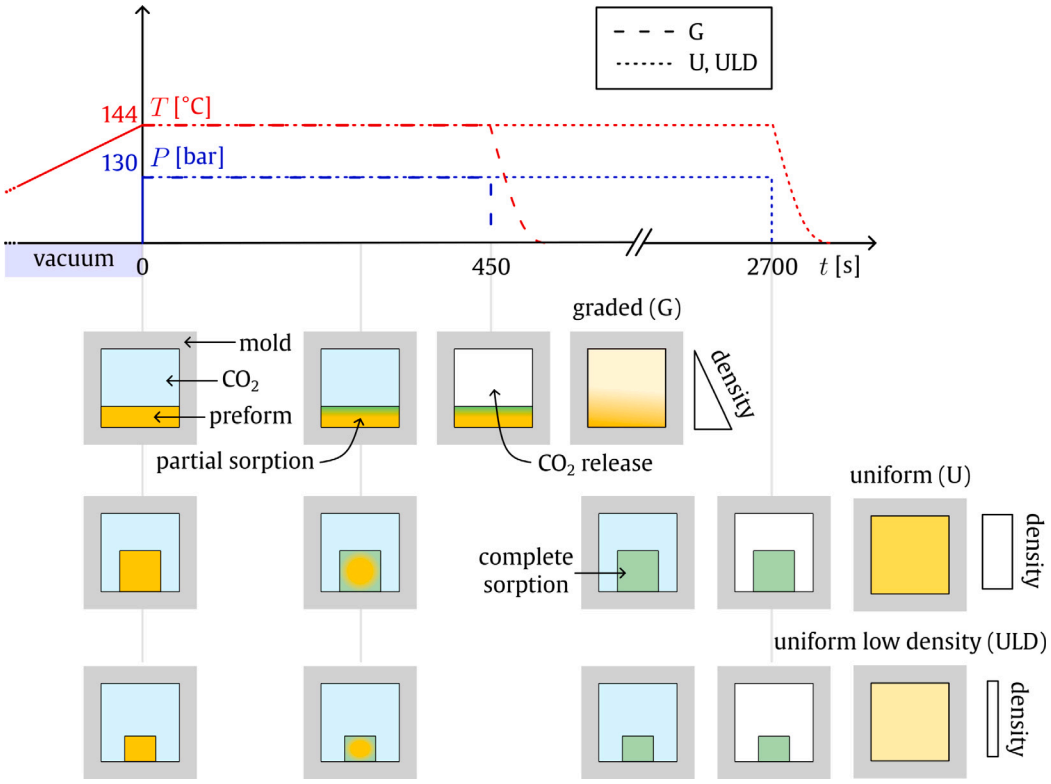

Fig. 1. Schematic of the production process of the graded (G), uniform (U) and uniform low density (ULD) foams used in this work. The different preforms are placed in identical cylindrical molds. The pressure vessel is then heated to a constant temperature of 144 °C under vacuum conditions. Once such a temperature is reached, a constant pressure of 130 bar CO_2 is applied. In the case of the preform p-G, the pressure is released after a sorption time of 450 s. Since the preform is only partially saturated with CO_2, it results in a foam with a density graded profile. In the case of the preforms p-U and p-ULD, the sorption step lasts 2700 s, allowing full CO_2 saturation of the preforms before pressure release, and the production of foams with uniform densities (U and ULD foams, respectively).

All the preforms are placed in the center of same cylindrical aluminum molds (to give foamed samples of same final geometry) with a diameter of 10 mm and a height of 10 mm. The mold is then inserted into the pressure vessel, and the temperature is increased to 144° C under vacuum conditions. Once the temperature is reached, the pressure of CO_2 is raised to 130 bar and maintained constant for a sorption time, t_s, which depends on the preform type: for types p-U and p-ULD, $t_s = 2700$ s, while for type p-G, $t_s = 450$ s. Subsequently, the pressure is released such that PDR = 500 bar/s, allowing the preforms to expand while being constrained by the mold, thereby producing the U, ULD, and G foams, respectively. An illustrative video of the preforms expansion is provided in Media 1.

Purposely, for the p-G preform 450 s are not sufficient to achieve a uniform (equilibrium) CO_2 concentration profile throughout the preform. At the pressure release, it expands with a designed density gradient and microstructural feature gradients arising from the non-equilibrium CO_2 concentration profile.

To measure the density (ρ_f) of the G, U, and ULD foams, we apply the buoyancy method along with the following equation:

$$\rho_f = \frac{m_a}{m_a - m_w}(\rho_w - \rho_a) + \rho_a \ , \tag{1}$$

where m_a is the weight of the foam in air, m_w is the weight of the foam in water, ρ_a is the density of air, and ρ_w is the density of water. At room temperature (23 ± 2° C), ρ_a = 1.20 kg/m^3 and ρ_w = 997.5 kg/m^3 [29]. The values m_a and m_w are measured using an analytical balance (model MS Semi-Micro, Mettler Toledo, Milan, Italy).

3. Synchrotron measurement and data analysis

SRμCT experiments are conducted at the ANATOMIX beamline [30,31] at the SOLEIL synchrotron radiation facility [32]. The experimental setup is illustrated in Fig. 2.

With an electron current of 500 mA in the SOLEIL storage ring and the ANATOMIX undulator X-ray source set to a magnetic gap of 6.4 mm, the polychromatic X-ray beam passes through a series of gold filters with a total thickness of 26 μm. The detector is an indirect system consisting of a single-crystal scintillator screen (cerium-doped lutetium aluminum garnet, supplier: Crytur, Turnov, Czech Republic), visible-light microscope optics (objective: Mitutoyo M PLAN APO 5x/NA0.14) and a scientific-grade CMOS camera (Hamamatsu model Orca Flash 4.0 V3), resulting in an effective pixel size of 1.3 μm and a field of view of 2.6 mm width and height. The exposure time for each projection radiography frame is set to 70 ms. The propagation distance between the tomography rotation axis and the scintillator was 60 mm. Tomography scans are taken with a continuous rotation and 2000 projection angles over 180 degrees; the total time for each scan is around 3 min. Tomographic reconstruction is performed using the standard data processing pipeline at the beamline, based on a Python script for pre-processing [34] and the PyHST2 program [35] as the backend, using a Paganin filter with a kernel length of 25 pixels.

Uniaxial compression experiments are performed using the mechanical testing device "Bulky", introduced by Pelerin et al. [33] and specifically developed for SRμCT. The device consisted of a lower moving grip attached to an in-line crosshead and an upper stationary grip, allowing for precise displacement controlled loading [33]. For these experiments, a 500 lb load cell was installed on the lower part of the frame, as depicted in Fig. 2, and connected to a dedicated conditioner, with alignment ensured through sample grips to provide reliable force monitoring.

Since all samples are 10 mm high, multiple scans are performed per sample (ranging from three to five, depending on the nominal strain level) in a column-wise fashion. Subsequent scans are conducted with an overlap of 125 voxels height (~0.16 mm) to enable reliable reconstruction of the entire height of the sample.

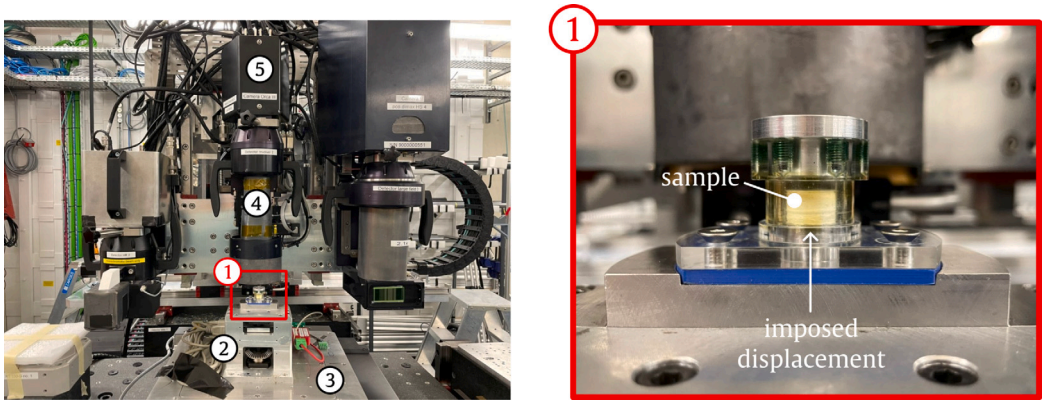

Fig. 2. Experimental setup at the ANATOMIX beamline [31] equipped with the uniaxial testing machine "Bulky" [33]. ① (zoomed in on the right) upper part of Bulky: for the compression testing, the foam sample is placed in a polymethyl methacrylate tube (which is transparent to X-rays) and the displacement is then imposed from the bottom [33]; ② lower part of Bulky; ③ rotating base; ④ detector optics; ⑤ camera.

Table 1
Strain steps adopted for G, U and ULD foams in the uniaxial compression test. The (u) means that it is an unloading phase which starts from the previous strain step. An empty space indicates that the test was not performed under this condition.

Sample \ Strain step [-]	0%	0.5%	1%	1.5%	5%	10%	5% (u)	20%	10% (u)	40%	20% (u)	50%	40% (u)	0% (u)
G	X		X	X	X	X	X	X	X	X	X	X		X
U	X	X		X	X	X	X	X	X	X	X	X		X
ULD	X	X	X	X	X	X	X	X	X	X	X	X	X	X

Each loading/unloading phase is conducted with a constant velocity of 60 μm/min. Due to the viscoelastic nature of the base material, investigated in [36], the resulting foam is also viscoelastic. Hence, after each loading/unloading phase, we allow the sample to relax and recover prior to acquisition. Since the time to relax and recover depends on the current engineering strain [37], the force-time curve is acquired and visualized in real-time to determine whether the material is sufficiently relaxed before initiating the acquisition. The duration of each experiment is approximately 10 h. In such a duration, considering that we do not irradiate the sample during relaxation/recovery steps, we assume that the effect of the X-ray radiation on the microstructure and mechanical properties of the foam is negligible [38].

Due to the complexity and length of each test, we tested one sample per type. With preliminary microscopy tests, we ensure that each of the samples was fully representative, in terms of density map and microstructural features, of the type of foams produced for this work. The densities of the tested G, U, and ULD foams were measured to be 342 kg/m^3, 302 kg/m^3, and 140 kg/m^3, respectively.

The sequence of strain steps is reported in Table 1 for all samples.

Data analysis was carried out using Fiji [39] and Python. For each strain level, virtual slices parallel to the vertical axis were extracted from the tomography data. This was done by stacking the volumes from each sub-scan of the sample in Fiji and then generating the corresponding slices (hereafter referred to as *vertical sections*). The resulting vertical sections were subsequently binarized using a Python-based segmentation algorithm (described in section 1 of *Supporting Information*).

Given the vertical section, the density profile is computed as follows: for each row—associated with a given height of the sample—we denote the pixel values after binarization as $p_i \in \{0,1\}$ such that $i = 1,\dots,N$, where $N = 1950$ represents the number of columns. The density ρ_j of row $j \in [1, M]$ (where M is the number of rows, which varies depending on the level of nominal strain) is computed as follows:

$$\rho_j = \frac{\rho^{PP}}{N}\sum_{i=1}^{N} p_i \ . \tag{2}$$

Then, we obtain the smoothed value of ρ_j, $\tilde{\rho}_j$, by applying a moving average centered on ρ_j with a window size of 200 pixels (which corresponds to ~253 μm). To perform such a smoothing operation, we use the function *uniform_filter1d* implemented in the SciPy Python library [40] with the default *reflect* option at the boundaries. This indicates that when $j \in [0,100]\cup[M-100, M]$ (up to ~127 μm from the boundaries) $\tilde{\rho}_j$ values are not fully reliable.

Given the same (segmented) vertical section, we compute the cell diameter and the characteristic cell circularity distributions by the following procedure (the pseudocode is provided in the section 2 of *Supporting Information*). We first define a rectangular region of interest (ROI) of size $s \times N$, where s is the step size. Within this ROI, we apply the watershed algorithm to identify individual cells and compute their areas and perimeters, excluding any cells that touch the borders of the ROI. From the values of the areas, A_i, we calculate the corresponding (equivalent) cell diameters, ϕ_i as:

$$\phi_i = 1.623\sqrt{\frac{4A_i}{\pi}} \ , \tag{3}$$

where the factor 1.623 accounts for the statistical bias arising from the fact that cells in a vertical section are generally not cut through their centers, causing their computed areas to underestimate the true areas (the derivation of such a factor is provided in ASTM D 3756-15 [41]). Then, we can compute the circularity of the cells as follows:

$$c_i = \frac{4\pi A_i}{P_i^2} \ , \tag{4}$$

where P_i represents the perimeter of the cell. All the values computed are then assigned to the z-coordinate (z) corresponding to the midpoint of the ROI. Next, we shift the ROI of $s/2$ and repeat the procedure until the whole vertical section is analyzed. The step size is constant and selected based on the foam type under consideration. For the graded foam, however, the step size is adjusted throughout the computation to account for the pronounced spatial variation in the microstructure.

In agreement with the results reported by Le Saux et al. [42] (see Table 1 therein), it should be noted that density and cell diameter obtained from 2D SRμCT image analysis are the only quantities that can be considered reliable both qualitatively and quantitatively, as they show consistency with corresponding 3D analyses. By contrast, while the observed trends in circularity can be regarded as qualitatively

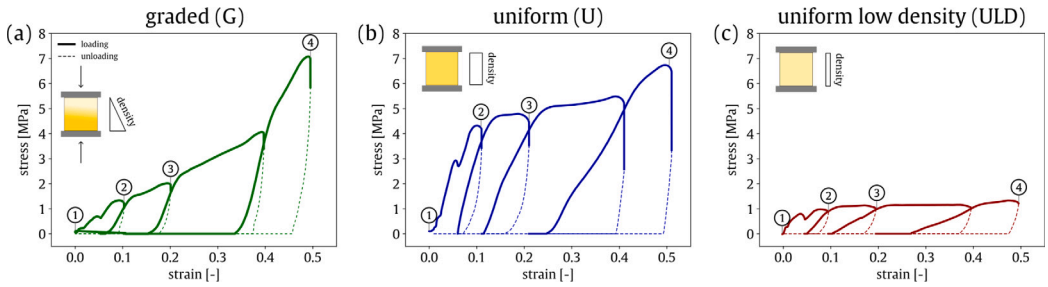

Fig. 3. Macroscopic compressive mechanical behavior of (a) the graded, (b) uniform and (c) uniform low density foams. The solid thick segments represents the loading curves, while the dashed thin ones the unloading curves. The circled numbers are referred to specific levels of strain (0%, 10%, 20% and 50%) of the vertical sections that will be analyzed in Figs. 5, 6, and 7.

meaningful, quantitative accuracy for foams can only be achieved through a full 3D analysis [42]. For this reason, a comprehensive 3D analysis will be the focus of future work.

4. Results and discussion

The results of the uniaxial compression tests of the G, U, and ULD foams are presented in Fig. 3.

From Fig. 3(a), it can be inferred that the macroscopic compressive mechanical behavior of the G foam differs qualitatively and quantitatively from that of the uniform foams, as evidenced by Fig. 3(b) and 3(c) and reported in the literature [5]. As described above, tests are conducted under loading (solid thick lines) and unloading (dashed thin lines) conditions; however, in this work, we will only consider the loading portion of the curve, while the unloading curves and the relaxed foam configurations will be the focus of a forthcoming paper. The loading curves highlight a major feature of the G foam: the absence of a plateau stress, which is conversely evident in the U and ULD foams. As will be shown in Fig. 5, this behavior can be attributed to the specific porous architecture at the microscale.

To further highlight the differences in macroscopic mechanical behavior, it is important to study and compare the energy absorption performance of the foams. Specifically, we compute the absorbed energy per unit volume (W) from the loading curves presented in Fig. 3, as follows:

$$W = \int_0^{\epsilon} \sigma(e)de \ , \tag{5}$$

and the efficiency, E [43],

$$E = \frac{\int_0^{\epsilon} \sigma(e)de}{\sigma(\epsilon)} \ . \tag{6}$$

The absorbed energy and efficiency curves are presented in Fig. 4(a) and (b) as functions of stress. The color gradient of each curve corresponds to the strain levels reported in the legend.

Even by observing such curves, the difference between the uniform foams and the graded one is straightforward. In the case of U and ULD, there is virtually a single stress value at which energy is absorbed (~5 MPa for the U foam and ~1 MPa for the ULD foam), which corresponds to the plateau stress dictated by the density. Conversely, G foams are characterized by a broad spectrum of stress values over which energy can be absorbed, ranging from 0.5 to 7 MPa. Similar arguments can be utilized to illustrate the differences observed in the efficiency curves. We can anticipate that a graded foam is particularly advantageous when energy needs to be absorbed in a real-life scenario of impact absorption, as the stress level is not known *a priori*. The absorbed energy and efficiency curves shown in Fig. 4(a) and (b) qualitatively align with the theoretical results presented by Koohbor and Kidane [4]; however, the quantitative theoretical modeling of the observed behavior of the graded foams will be the focus of a forthcoming paper.

The macroscopic mechanical results can be better understood in light of the microstructural features, which are depicted in Figs. 5, 6, 7.

The vertical sections of the G foam at four selected strain levels (0%, 10%, 20%, and 50%) are shown in Fig. 5, together with the corresponding density profiles ($\tilde{\rho}_j$ as a function of the z-coordinate, computed as described in Section 3). In the reference configuration (i.e., 0% strain), a clear density gradient is observable, accompanied by both a microstructural anisotropy and a cell size gradient of the cells, arising from the preferential expansion direction during graded foam production. Upon compression, collapse bands develop predominantly in the upper part of the sample, which corresponds to the region of lowest density. At 50% strain, it is evident that densification progresses from the top toward the bottom of the specimen, i.e., from the low-density to the high-density region. This gradient-driven collapse is consistent with the gradual stress increase observed in Fig. 3(a). As expected, this behavior contrasts with the compressive response of the U and ULD foams. For proper comparison, Figs. 6 and 7 present the reference and deformed configurations of the U and ULD foams at the same strain levels, along with their respective density profiles. In the U foam, densification occurs in a nearly homogeneous manner across the sample height, as evidenced by the evolution of its density profiles. In contrast, the ULD foam exhibits highly localized deformation, with pronounced density peaks emerging during compression.

Fig. 8 further highlights these findings: while the U foam maintains a relatively uniform deformation at low strain, the ULD foam exhibits severe local displacements and distortions as early as 10% strain.

To further investigate the micromechanisms underlying the formation of densification regions, we present in Fig. 9 the details of the compression bands observed at strains of up to 10% in the G and ULD foams.

In the G foam, at a nominal strain of 1.5%, a collective buckling of the most elongated cells in the low-density region can be observed, while the underlying cells remain almost undeformed. As the strain increases, the deformation of these elongated cells becomes progressively more severe, whereas the onset of buckling in the lower cells is only noticeable at around 10% nominal strain. This indicates a pronounced strain localization within the low-density portion of the graded foam. This observation is consistent with the right panel of Fig. 9, which highlights the collapse of a specific region in the ULD foam. This region, characterized by a lower local density (thinner struts and walls), is mechanically weaker and, therefore, less capable of sustaining loads compared to its surroundings. Consequently, structural collapse initiates in this localized low-density zone, giving rise to denser bands in the same region. This behavior aligns with the previous findings of Elliott et al. [21].

To further support the aforementioned observations on density and to relate them to microstructural details, we analyze (i) the cell diameter and (ii) the cell circularity across the foams at the four strain levels considered in Figs. 5, 6, and 7. In Fig. 10(a)–(c), we illustrate an example of the cell diameter distributions at 0% strain and at z =

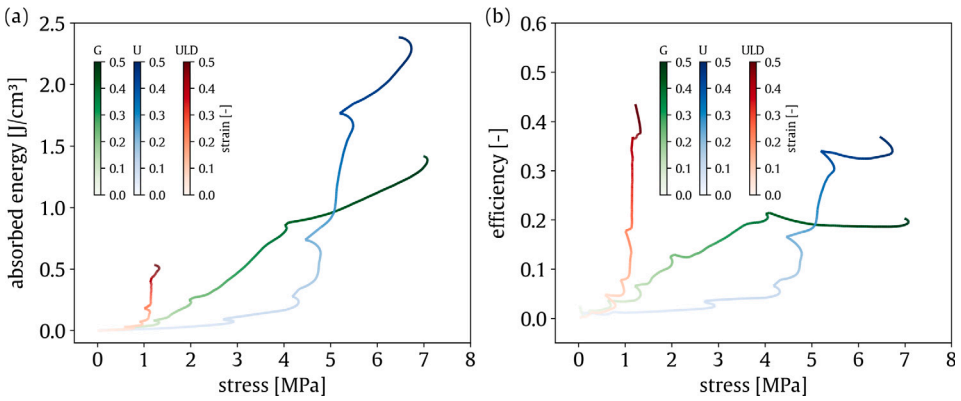

Fig. 4. Energy absorption performance of the G, U and ULD foams with respect to stress. Strain is also reported using proper colorbars. (a) Absorbed energy (Eq. (5)). (b) Efficiency (Eq. (6)).

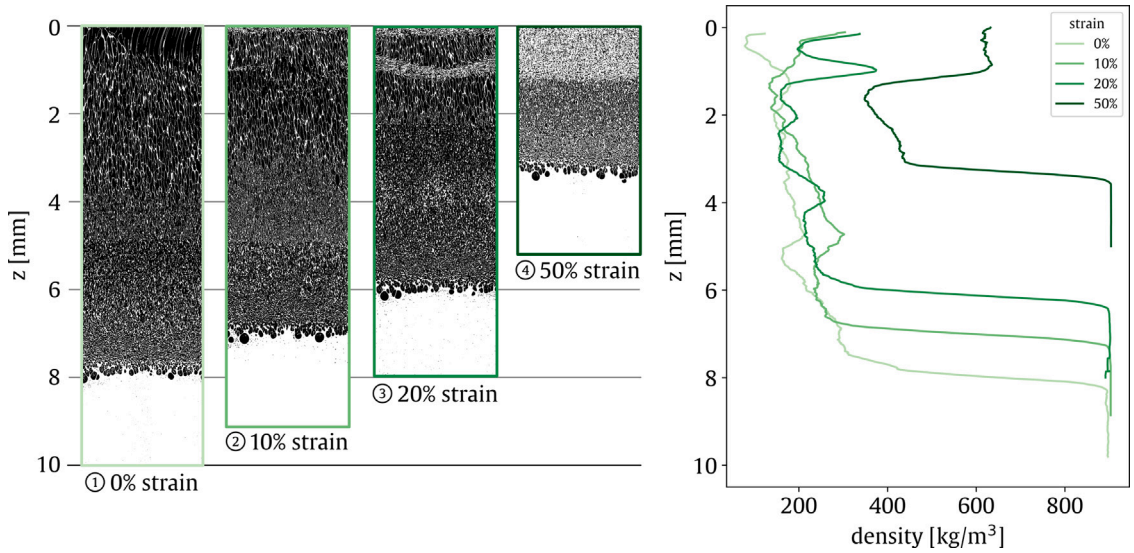

Fig. 5. On the left, the binarized vertical sections of the graded foam at 0% (reference configuration), 10%, 20% and 50% strain. White: material (PP), black: cell space. Underlaid, a grid with the z-coordinate is in correspondence with the figure on the right, which reports the density profile (computed as described in Section 3) as a function of the z-coordinate. The levels of strain are in correspondence with the stress levels of Fig. 3(a) through the circled numbers.

0.78 mm to motivate the choice of statistical descriptors that will be employed in the subsequent analysis.

As observed, the resulting distributions in all cases deviate substantially from both lognormal and Gaussian shapes. Due to their pronounced asymmetry, we adopt the median as a representative statistical indicator. To provide a smooth representation of the underlying probability structure, we will additionally employ kernel density estimation (KDE) to approximate the discrete probability density function.

Figs. 11 and 12 show the KDE surfaces of the diameter and circularity probability density functions, respectively, for all foams. The data are organized with foam types along the rows and strain levels (0%, 10%, 20%, and 50%) along the columns.

As expected, for the reference configuration of the G foam, the KDE surfaces exhibit significant variation along the z direction for both cell diameter (Fig. 11) and circularity (Fig. 12). Specifically, cell size decreases and circularity increases toward the higher-density region. Under compression, cells in the low-density region progressively shrink, shifting the diameter KDE surface to the left and making it resemble a more lognormal distribution. Simultaneously, circularity increases, causing the corresponding KDE surface to shift to the right. In contrast, the uniform foams (U and ULD) show much smaller variations in their KDE surfaces along the sample height in both the reference and deformed configurations. For these foams, the KDE surfaces of both diameter and circularity become increasingly lognormal under compression, with the distributions shifting to the left.

These observations are further supported by monitoring the evolution of the cell diameter (median) and circularity (median) with increasing strain for the different foams, as shown in Fig. 13(a)–(f). For the G foam (Fig. 13(a) and (d)), the reference configuration exhibits a pronounced gradient in cell diameter (circularity) —from about 110 μm (0.4) in the low-density region to about 20 μm (0.95) in the high-density region—alongside the density gradient. As compressive strain increases, the larger cells in the low-density region collapse more readily than the smaller cells located closer to the high-density region. Additionally, due to the progressive buckling, the circularity of larger, initially strongly elongated cells tends to increase. Because deformation localizes within the first few millimeters of the sample, the cells in the higher-density region remain nearly unchanged up to 50% strain; this is reflected, indeed, in the cell diameter and circularity profiles at z-coordinates between 5 and 8 mm, which shift almost horizontally with increasing strain. The results regarding the cell diameter and circularity in Fig. 13(b), (c), (e) and (f), also support the findings on the density in Figs. 6 and 7. First, for both U and ULD foams, the variation in cell size (Fig. 13(b) and (c)) and circularity (Fig. 13(e) and (f)) in the reference configuration, as well as when increasing compressive strain, is small compared to the variation of the same statistical indicators of the G foam.

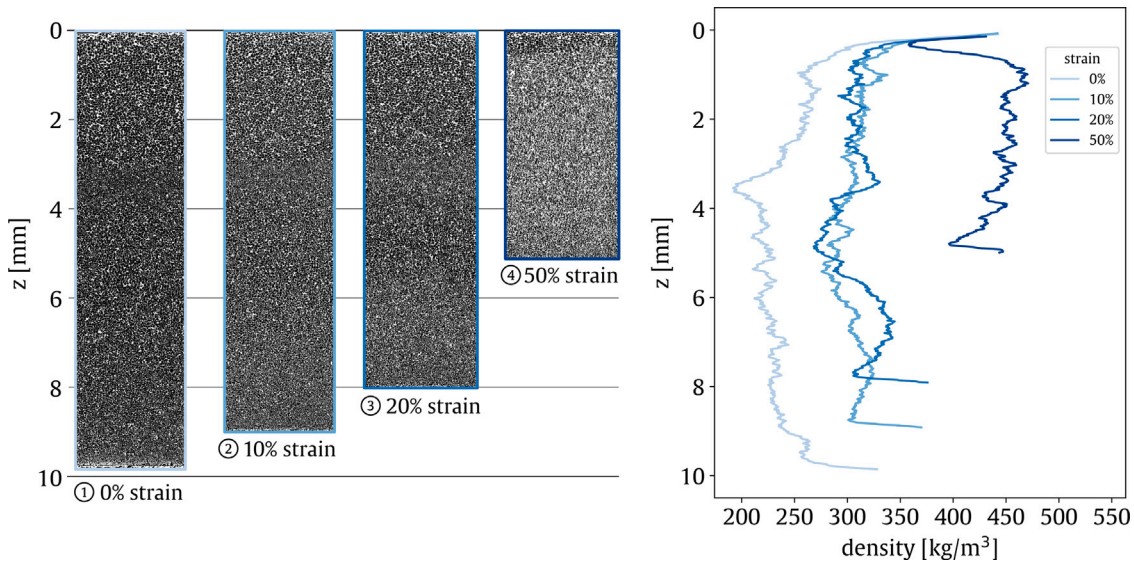

Fig. 6. On the left, the binarized vertical sections of the uniform foam at 0% (reference configuration), 10%, 20% and 50% strain. White: material(PP), black: cell space. Underlaid, a grid with the z-coordinate is in correspondence with the figure on the right, which reports the density profile (computed as described in Section 3) as a function of the z-coordinate and of the strain. The levels of strain are in correspondence with the stress levels of Fig. 3(b) through the circled numbers.

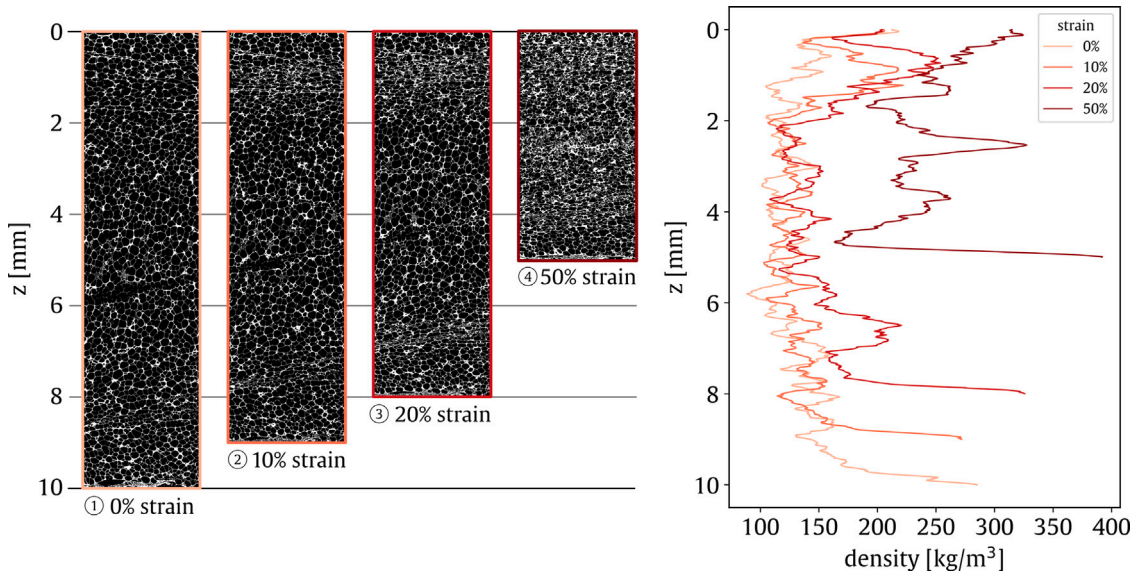

Fig. 7. On the left, the binarized vertical sections of the uniform low density foam at 0% (reference configuration), 10%, 20% and 50% strain. White: material (PP), black: cell space. Underlaid, a grid with the z-coordinate is in correspondence with the figure on the right, which reports the density profile (computed as described in Section 3) as a function of the z-coordinate and of the strain. The levels of strain are in correspondence with the stress levels of Fig. 3(c) through the circled numbers.

Focusing on the U foam (Fig. 13(b)), a local minimum in the cell diameter is observed at approximately 3.5 mm in the reference configuration, consistent with the features shown in Fig. 6. As strain increases, the overall shape of the cell diameter profile remains largely unchanged, and the minimum cell diameter does not decrease further. This indicates that, in the present case, the variation in cell size is insufficient to drive or guide foam collapse, suggesting instead that density is the dominant factor governing the macroscopic mechanical response. As expected, Fig. 13(e) shows that increasing strain leads to more elongated cells oriented perpendicular to the loading direction, which is reflected in a reduction in circularity.

For the ULD foam (Fig. 13(c)), increasing strain leads to the formation of localized minima in the cell diameter profiles relative to the reference configuration. At 10% strain, these minima begin to appear, indicating regions where cells start to undergo significant size reduction. From 20% strain, the minima become more pronounced, reflecting a clearer localization of deformation. These local reductions in cell diameter correspond directly to the collapse bands observed in Fig. 7. The onset and evolution of these minima are also clearly reflected in the circularity profiles at different strain levels in Fig. 13(f). As a collapse band develops, cell shapes rapidly transition from nearly

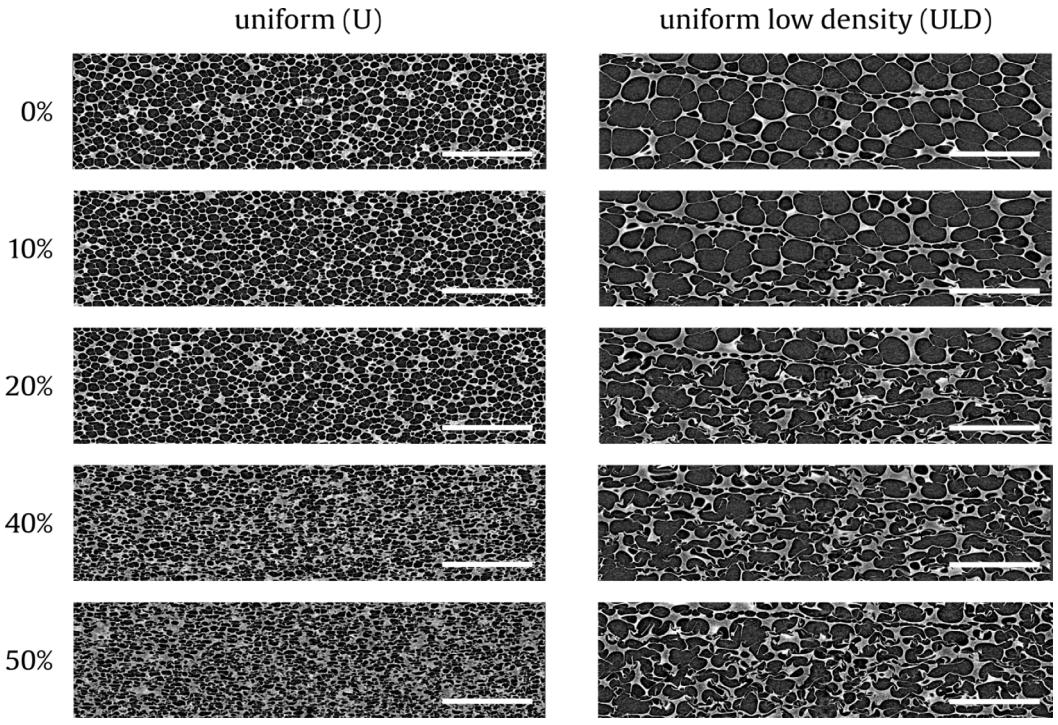

Fig. 8. Details of the progressive deformation of U (left) and ULD (right) foams. White bar is 500 μm.

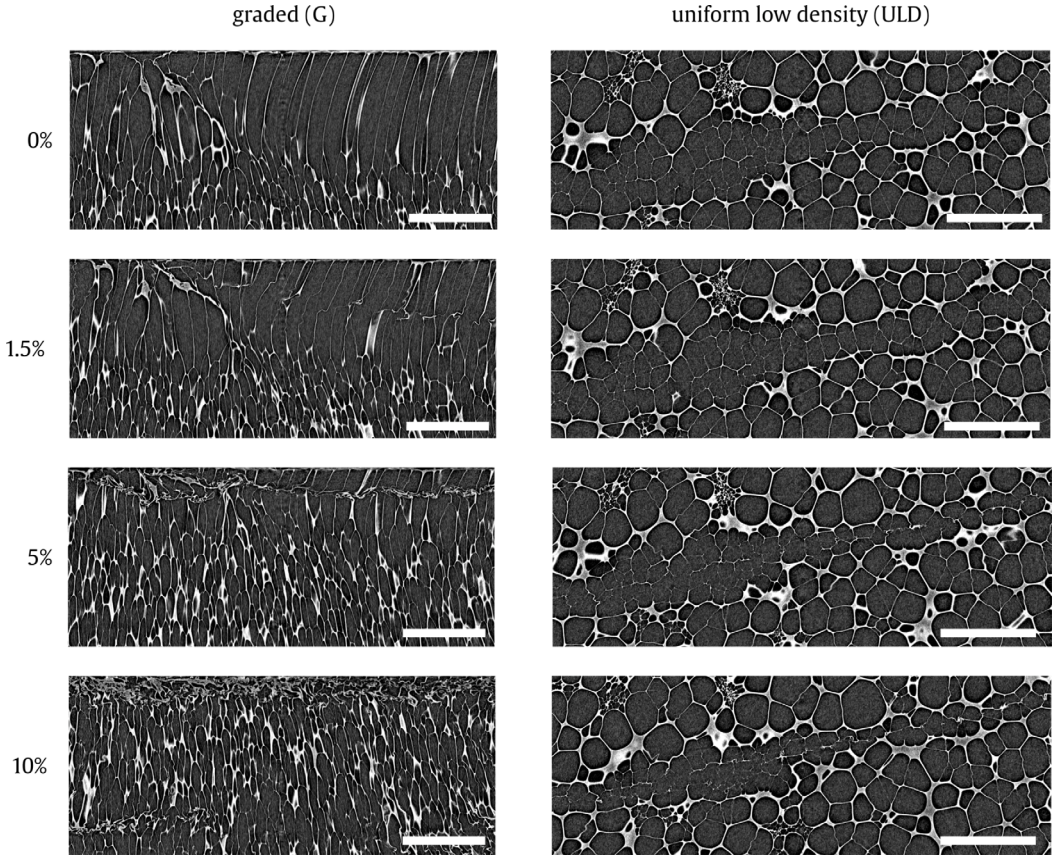

Fig. 9. Details of the collapse bands in the G foam (left) and the ULD foam (right) as a function of the strain of the sample. White bar is 500 μm.

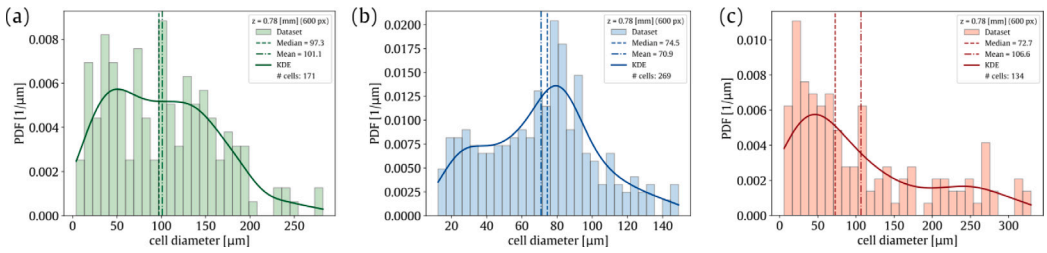

Fig. 10. Examples of typical probability density functions obtained for cell diameters. (a) graded foam; (b) uniform foam; (c) uniform low density foam. The kernel density estimation (KDE), mean and median are also reported. Note that all the distributions are obtained at $z = 0.78$ mm (which corresponds to 600 pixels) and at 0% strain.

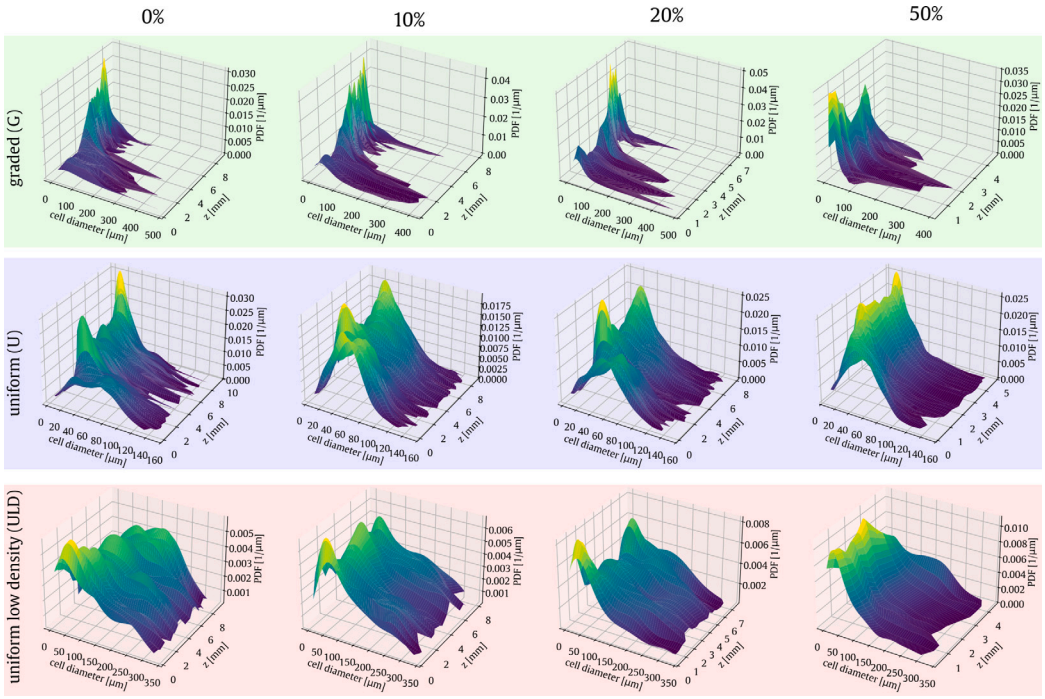

Fig. 11. Kernel density estimation (KDE) surfaces of cell diameter derived from local distributions computed within windows (centered at each z-coordinate) along the height of the sample. The layout is organized row-wise by foam type (graded, uniform, and uniform low density) and column-wise by applied strain (0%, 10%, 20%, and 50%). Specific scaling is used to improve the visibility of distribution features.

circular to elliptical, with elongation perpendicular to the loading direction, thereby locally increasing the microstructural compliance.

Additional information on the onset of buckling and bending could be obtained through the analysis of other statistical indicators, such as cell shape, spatial orientation, or sphericity. However, we would like to remark that the analysis performed is in 2D, and according to the literature results, the aforementioned statistical indicators are quantitatively reliable only with a 3D image analysis [42].

5. Conclusion and perspectives

Recent advances in foaming technologies have enabled the production of novel graded foams, which exhibit remarkable properties, particularly in energy absorption. Nevertheless, the relationship between their microstructure and macroscopic mechanical behavior remains poorly understood. To address this gap, we design and fabricate a graded foam with a unidirectional density gradient and investigate its uniaxial compressive behavior via *in-situ* SRµCT. For proper comparison, we also investigate the mechanical response of two uniform foams produced for this purpose. In agreement with theoretical predictions from the literature, the graded foam displays markedly different macroscopic mechanical behavior compared to uniform foams, as reflected in the peculiar shape of its energy absorption (or efficiency) versus stress curve. By computing density, cell diameter, and circularity profiles as a function of both strain and sample height, we show that this behavior arises from the progressive and highly localized collapse of the microstructure, which is guided by the density gradient. In contrast, the uniform foams exhibit either nearly homogeneous compression or localized collapse bands, both of which lead to the well-established macroscopic response typical of standard commercial foams. These findings highlight the potential of graded foams for tailored energy absorption applications, as the collapse process can be deliberately guided through a purposely designed 3D density map.

To advance understanding in this field, future work should focus on several key directions. As an example, more efficient segmentation algorithms are needed to capture the sharp morphological variations characteristic of graded foams. Such tools would enable a quantitative analysis of all microstructural statistical parameters and their evolution under increasing strain. Additionally, the development of multiscale models capable of predicting the progressive, density-graded collapse of the microstructure would represent a fundamental step toward a deeper understanding of the microstructure–property relationships in graded foams.

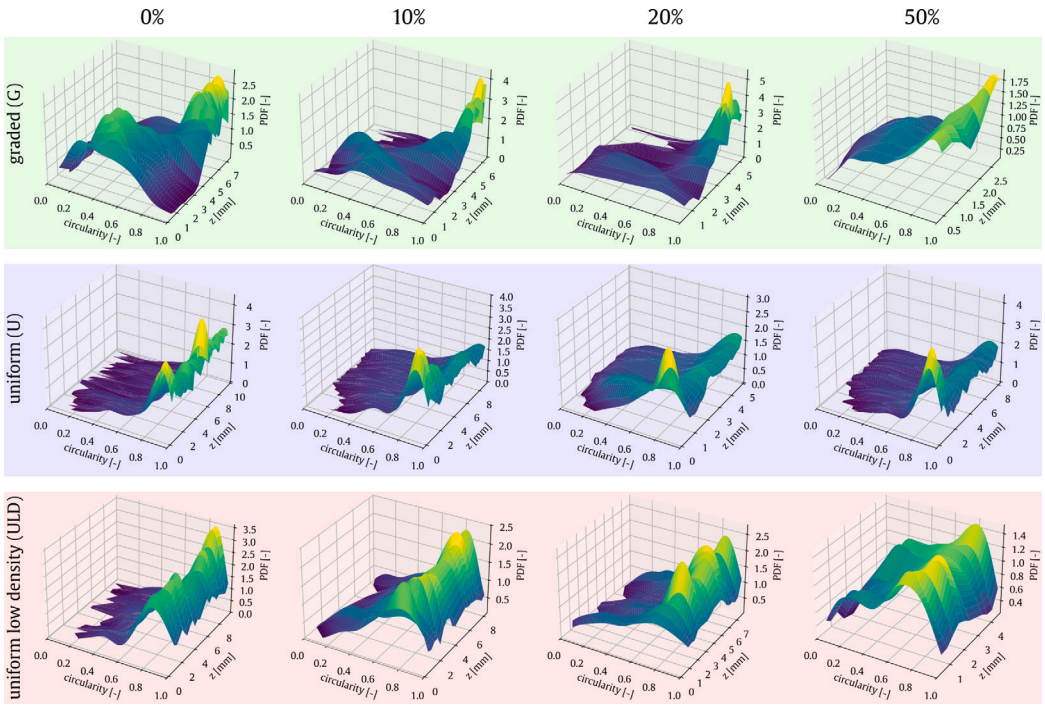

Fig. 12. Kernel density estimation (KDE) surfaces of cell circularity derived from local distributions computed within windows (centered at each z-coordinate) along the height of the sample. The layout is organized row-wise by foam type (graded, uniform, and uniform low density) and column-wise by applied strain (0%, 10%, 20%, and 50%). Specific scaling is used to improve the visibility of distribution features.

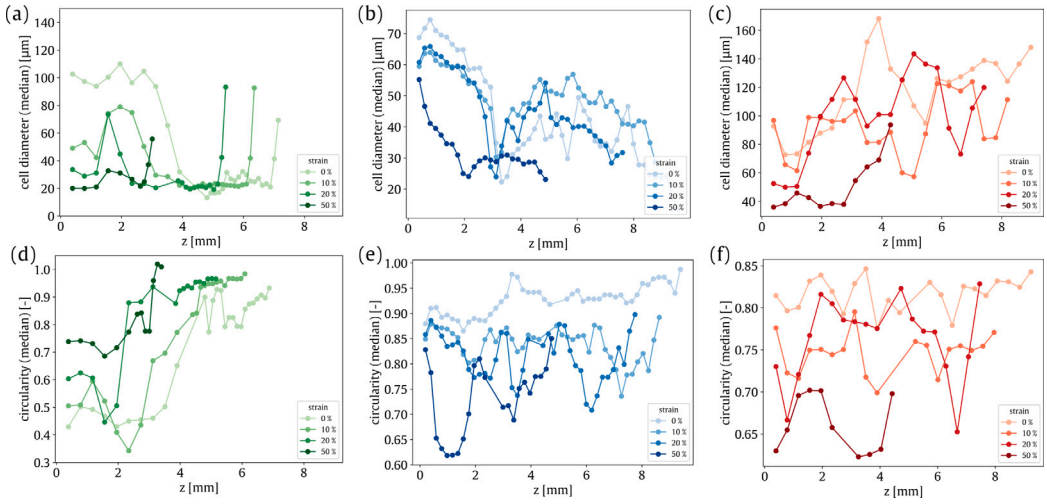

Fig. 13. Cell diameter (median) and circularity (median) as functions of the z-coordinate at 0% (reference configuration), 10%, 20%, and 50% strain. At each z-position, the reported values correspond to the median of the underlying cell diameter and circularity distributions. Subfigures (a) and (d) correspond to the graded (G) foam; subfigures (b) and (e) to the uniform (U) foam; and subfigures (c) and (f) to the uniform low density (ULD) foam. Note that different scales are used for cell diameter and circularity in the figures of the panel to better emphasize variations across foams and strain levels.

CRediT authorship contribution statement

Paolo Iaccarino: Writing – review & editing, Writing – original draft, Visualization, Validation, Supervision, Software, Resources, Methodology, Investigation, Formal analysis, Data curation, Conceptualization. **Clément Rey:** Writing – original draft, Visualization, Validation, Software, Data curation. **Lorenzo Miele:** Writing – review & editing, Writing – original draft, Visualization, Validation, Software, Data curation. **Victor Okumko:** Writing – original draft, Investigation. **Mario Scheel:** Writing – review & editing, Supervision, Software, Resources, Methodology, Investigation, Funding acquisition, Formal analysis, Data curation. **Timm Weitkamp:** Writing – review & editing, Validation, Supervision, Resources, Methodology, Funding acquisition. **Henry Proudhon:** Writing – review & editing, Supervision, Software, Resources, Methodology. **Ferdinando Auricchio:** Writing – review & editing, Writing – original draft, Visualization, Resources, Methodology, Conceptualization. **Ernesto Di Maio:** Writing – review & editing, Writing – original draft, Visualization, Validation, Methodology, Investigation, Funding acquisition, Conceptualization. **Andrei Constantinescu:** Writing – review & editing, Writing – original draft, Visualization, Validation, Supervision, Resources, Project administration, Investigation, Funding acquisition, Formal analysis, Data curation, Conceptualization.

Declaration of competing interest

The authors declare the following financial interests/personal relationships which may be considered as potential competing interests: Andrei Constantinescu reports was provided by Polytechnic University. If there are other authors, they declare that they have no known competing financial interests or personal relationships that could have appeared to influence the work reported in this paper.

Acknowledgments

The authors thank Synchrotron SOLEIL for the ANATOMIX beamline time (proposal n° 20241288, *Investigating the micromechanics of graded polymer foams*, main proposer: Paolo Iaccarino). ANATOMIX is an Equipment of Excellence (EQUIPEX) funded by the *Investments for the Future* program of the ANR, project *NanoimagesX*, grant no. ANR-11-EQPX-0031. The authors also thank Andrew King and Guillaume Daniel (Synchrotron SOLEIL) for their assistance in the installation of Bulky and Pasquale Strazzullo (University of Naples Federico II) for his help in realizing Media 1 for the visualization of the preforms expansion.

Appendix A. Supporting information

Additional details on the pseudocodes are available in the *Supporting Information* file.

Supplementary material related to this article can be found online at https://doi.org/10.1016/j.polymertesting.2026.109107.

Data availability

Data will be made available on request.

References

[1] P. Iaccarino, E. Maresca, S. Morganti, F. Auricchio, E. Di Maio, Topologically optimized graded foams, Adv. Eng. Mater. 26 (11) (2024) 2301798.
[2] B. Koohbor, S. Ravindran, A. Kidane, In situ deformation characterization of density-graded foams in quasi-static and impact loading conditions, Int. J. Impact Eng. 150 (2021) 103820.
[3] M. Smeets, B. Koohbor, G. Youssef, Quasi-static mechanical response of density-graded polyurea elastomeric foams, ACS Appl. Polym. Mater. 5 (4) (2023) 2840–2851.
[4] B. Koohbor, A. Kidane, Design optimization of continuously and discretely graded foam materials for efficient energy absorption, Mater. Des. 102 (2016) 151–161.
[5] L. Gibson, M. Ashby, Cellular Solids, Structure and Properties, second ed. Cambridge University Press, 1997.
[6] H. Zhou, Y. Wang, X. Wang, Z. Zhao, G. Ma, Energy absorption of graded foam subjected to blast: a theoretical approach, Mater. Des. 84 (2015) 351–358.
[7] M. Liang, Z. Li, F. Lu, X. Li, Theoretical and numerical investigation of blast responses of continuous-density graded cellular materials, Compos. Struct. 164 (2017) 170–179.
[8] D. Chen, S. Kitipornchai, J. Yang, Dynamic response and energy absorption of functionally graded porous structures, Mater. Des. 140 (2018) 473–487.
[9] V. Gupta, A. Kidane, Designing density-graded cellular materials for tailored constitutive response, Compos. Part B: Eng. 287 (2024) 111793.
[10] V. Gupta, A. Kidane, M. Sutton, Dynamic characteristics of density-graded cellular materials for impact mitigation, Int. J. Solids Struct. 296 (2024) 112816.
[11] Y. Ding, S. Wang, Z. Sun, V. Shim, Density-graded voronoi honeycombs–a local transversely isotropic description, Int. J. Solids Struct. 285 (2023) 112555.
[12] B. Chang, Z. Zheng, Y. Zhang, Y. Zhang, K. Zhao, J. Yu, Crashworthiness design of graded cellular materials: Experimental verification of the backward design strategy, Int. J. Impact Eng. 171 (2023) 104366.
[13] V. Gupta, A. Kidane, Impact response of additively manufactured density-graded open-cell foams, Int. J. Impact Eng. 195 (2025) 105127.
[14] M. Trofa, E. Di Maio, P.L. Maffettone, Multi-graded foams upon time-dependent exposition to blowing agent, Chem. Eng. J. 362 (2019) 812–817.
[15] X. Zhu, Z. Cheng, Y. Chen, Thickness measurement of cell walls of closed-cell foams in micro-ct images, J. Microsc. 291 (2) (2023) 145–155.
[16] T. Ono, S. Samitsu, M. Hazutani, S. Ata, Structural characterization of hierarchical polymer foams by combining X-ray micro-computed tomography and scanning electron microscopy, Polym. Test. 140 (2024) 108580.
[17] D.S. Bolintineanu, R. Waymel, H. Collis, K.N. Long, E.C. Quintana, S.L. Kramer, Anisotropy evolution of elastomeric foams during uniaxial compression measured via in-situ X-ray computed tomography, Materialia 18 (2021) 101112.
[18] I. Koch, G. Preiß, M. Müller-Pabel, B. Grüber, M. Gude, Analysis of density-dependent cell structure of epp bead foams under compression, Exp. Mech. (2025) 1–10.
[19] M. Foster, K. Steirer, J. Bernstein, M. Herynk, L. Lamberson, Influence of pore geometry and distribution on buckling under micro computed tomography, Polymer (2025) 128434.
[20] P. Cloetens, W. Ludwig, J. Baruchel, D. Van Dyck, J. Guigay J. Van Landuyt, M. Schlenker, Holotomography: Quantitative phase tomography with micrometer resolution using hard synchrotron radiation X rays, Appl. Phys. Lett. 75 (19) (1999) 2912–2914.
[21] J. Elliott, A. Windle, J. Hobdell, G. Eeckhaut, R. Oldman, W. Ludwig, E. Boller, P. Cloetens, J. Baruchel, In-situ deformation of an open-cell flexible polyurethane foam characterised by 3d computed microtomography, J. Mater. Sci. 37 (2002) 1547–1555.
[22] S. Youssef, E. Maire, R. Gaertner, Finite element modelling of the actual structure of cellular materials determined by X-ray tomography, Acta Mater. 53 (3) (2005) 719–730.
[23] J. Adrien, E. Maire, N. Gimenez, V. Sauvant-Moynot, Experimental study of the compression behaviour of syntactic foams by in situ X-ray tomography, Acta Mater. 55 (5) (2007) 1667–1679.
[24] S. Roux, F. Hild, P. Viot, D. Bernard, Three-dimensional image correlation from X-ray computed tomography of solid foam, Compos. Part A: Appl. Sci. Manuf. 39 (8) (2008) 1253–1265.
[25] H. Chai, H. Li, X. Xiao, J. Huang, S. Luo, Correlation between cell wall buckling and deformation banding in a closed-cell foam, Scr. Mater. 170 (2019) 177–182.
[26] H. Chai, Z. Xie, X. Xiao, H. Xie, J. Huang, S. Luo, Microstructural characterization and constitutive modeling of deformation of closed-cell foams based on in situ X-ray tomography, Int. J. Plast. 131 (2020) 102730.
[27] L. Miele, E. Di Lorenzo, C. Guissart, E. Di Maio, Liquid foaming of tpu with methylal, Heliyon 10 (12) (2024).
[28] P. Iaccarino, P. Sisti, D. Ferri, E. Di Maio, Insights into the quasi-static mechanics of transversely isotropic polymer foams, 2025, http://dx.doi.org/10.2139/ssrn.5333828, Available at SSRN.
[29] R. Weast, Handbook of Chemistry and Physics, fifty-third ed. Chemical Rubber Pub., 1972, URL https://books.google.it/books?id=aXHKtAEACAAJ,
[30] T. Weitkamp, M. Scheel, J. Giorgetta, V. Joyet, G. Cauchon V. Le Roux, T. Moreno, F. Polack, A. Thompson, J. Samama, The tomography beamline ANATOMIX at Synchrotron SOLEIL, J. Phys.: Conf. Ser. 849 (2017) 012037, IOP Publishing.
[31] T. Weitkamp, M. Scheel, J. Perrin, G. Daniel, A. King, V. Le Roux, J.-L. Giorgetta, A. Carcy, F. Langlois, K. Desjardins, et al., Microtomography on the ANATOMIX beamline at Synchrotron SOLEIL, J. Phys.: Conf. Ser. 2380 (2022) 012122, IOP Publishing.
[32] J. Susini, J.-M. Cassagne, B. Gagey, A. Nadji, A. Taleb, A. Thompson, J. Daillant, A brief introduction to the Synchrotron SOLEIL and its upgrade programme, Eur. Phys. J. Plus 139 (1) (2024) 80.
[33] M. Pelerin, A. King, L. Laiarinandrasana, H. Proudhon, Development of a versatile mechanical testing device for in situ synchrotron tomography and diffraction experiments, Integr. Mater. Manuf. Innov. 8 (2019) 378–387.
[34] A. King, N. Guignot, J.-P. Deslandes, M. Pelerin, I. Joosten, D. De Looff, J. Li, L. Bertrand, E. Rosenberg, A. Dewaele, et al., Recent tomographic imaging developments at the psiche beamline, Integr. Mater. Manuf. Innov. 8 (4) (2019) 551–558.
[35] A. Mirone, E. Brun, E. Gouillart, P. Tafforeau, J. Kieffer, The pyhst2 hybrid distributed code for high speed tomographic reconstruction with iterative reconstruction and a priori knowledge capabilities, Nucl. Instrum. Methods Phys. Res. Sect. B: Beam Interactions Mater. Atoms 324 (2014) 41–48.
[36] P. Iaccarino, E. Di Maio, A. Constantinescu, F. Auricchio, Thermo-rheologically complex polymers: multiaxial constitutive modeling, numerical implementation and experimental validation, Polym. Test. 150 (2025) 108937.
[37] A. Greco, F. Lionetto, The influence of the stress relaxation and creep recovery times on the viscoelastic properties of open cell foams, Polym. Eng. Sci. 49 (6) (2009) 1142–1150.
[38] A.K. Landauer, Z. Tsinas, O.L. Kafka, N.H. Moser, J.L. Glover, A.M. Forster, Unintended consequences: Assessing thermo-mechanical changes in vinyl nitrile foam due to micro-computed X-ray tomographic imaging, Mater. Des. 235 (2023) 112381.
[39] J. Schindelin, I. Arganda-Carreras, E. Frise, V. Kaynig, M. Longair, T. Pietzsch, S. Preibisch, C. Rueden, S. Saalfeld, B. Schmid, et al., Fiji: an open-source platform for biological-image analysis, Nature Methods 9 (7) (2012) 676–682.

[40] P. Virtanen, R. Gommers, T.E. Oliphant, M. Haberland, T. Reddy, D. Cournapeau, E. Burovski, P. Peterson, W. Weckesser, J. Bright, S.J. van der Walt, M. Brett, J. Wilson, K.J. Millman, N. Mayorov, A.R. J. Nelson, E. Jones, R. Kern, E. Larson, C.J. Carey, İ. Polat, Y. Feng, E.W. Moore, J. VanderPlas, D. Laxalde, J. Perktold, R. Cimrman, I. Henriksen, E.A. Quintero, C.R. Harris, A.M. Archibald, A.H. Ribeiro, F. Pedregosa, P. van Mulbregt, SciPy 1.0 Contributors SciPy 1.0: Fundamental algorithms for scientific computing in Python, Nature Methods 17 (2020) 261–272, http://dx.doi.org/10.1038/s41592-019-0686-2.

[41] ASTM D3756-15, Standard test method for evaluating cell size of rigid cellular plastics, 2015, ASTM International, West Conshohocken, PA.

[42] M. Le Saux, J.-B. Le Bail, J. Becker, C. Caër, P. Charrier, V. Le Saux, L. Maheo, Y. Marco, Statistical characterization of microcellular polyurethane foams microstructure based on 2D and 3D image analysis, J. Cell. Plast. 59 (5–6) (2023) 395–417.

[43] M. Avalle, G. Belingardi, R. Montanini, Characterization of polymeric structural foams under compressive impact loading by means of energy-absorption diagram, Int. J. Impact Eng. 25 (5) (2001) 455–472.